Special Issue Article

Double pulsed field gradient (double-PFG) MR imaging (MRI) as a means to measure the size of plant cells[†]

E. Özarslan,[a,b]* M. E. Komlosh,[a,b] M. J. Lizak,[c] F. Horkay[a] and P. J. Basser[a]

Measurement of diffusion in porous materials and biological tissues with the pulsed field gradient (PFG) MR techniques has proven useful in characterizing the microstructure of such specimens noninvasively. A natural extension of the traditional PFG technique comprises multiple pairs of diffusion gradients. This approach has been shown to provide the ability to characterize anisotropy at different length scales without the need to employ very strong gradients. In this work, the double-PFG imaging technique was used on a specimen involving a series of glass capillary arrays with different diameters. The experiments on the phantom demonstrated the ability to create a quantitative and accurate map of pore sizes. The same technique was subsequently employed to image a celery stalk. A diffusion tensor image (DTI) of the same specimen was instrumental in accurately delineating the regions of vascular tissue and determining the local orientation of cells. This orientation information was incorporated into a theoretical double-PFG framework and the technique was employed to estimate the cell size in the vascular bundles of the celery stalk. The findings suggest that the double-PFG MRI framework could provide important new information regarding the microstructure of many plants and other food products. Copyright © 2012 John Wiley & Sons, Ltd.

Keywords: diffusion; plant cell; pulsed field gradient; microscopic; anisotropy; cell size; general gradient waveform; double; multiple; wavevector

Introduction

The nuclear magnetic resonance (NMR) signal can be sensitized to diffusive motion of spin bearing molecules, e.g., via the application of pulsed field gradients (PFGs).[1] When the specimen contains pores that restrict the random motion of these molecules, the resulting signal possesses information about the underlying microstructure of the porous medium. Consequently, diffusion NMR provides a means to probe microscopic length scales, which are impossible to resolve using conventional magnetic resonance imaging (MRI).

The most widely-used approach to provide diffusion sensitization involves the application of a single pair of PFGs. These "single-PFG" acquisitions have been successful in characterizing many useful features of the porous specimens. However, as pore size gets smaller, the experiment demands stronger gradient strengths to characterize the diffusion process.

It has been realized since '90s that when multiple diffusion gradient pulse pairs are employed,[2] the dependence of the signal on the angle between the different gradient vectors could yield information that is descriptive of the particular diffusional motion and the underlying porous structure.[3,4] Such experiments can be regarded as multidimensional acquisitions yielding information about correlations of motion during different encoding intervals.[5] If the diffusion process can be assumed to be locally Gaussian, a two-dimensional Laplace transform can be utilized to produce maps of diffusion coefficients illustrating the motional correlation during the separate encoding intervals. Such an analysis has been performed on chive samples.[6]

In recent years, the multiple-PFG extensions of the single-PFG experiments have attracted a great deal of interest in the context of restricted (non-Gaussian) diffusion. It was shown that the non-monotonicity of the signal characteristic of the so-called "diffusion-diffraction" phenomenon in single-PFG experiments[7] is replaced by zero-crossings when an even number of gradient pulse pairs are employed, making the phenomenon robust to microscopic heterogeneity of the examined specimen.[8]

When the angle between the gradients of a multiple-PFG sequence is varied, the signal can be sensitized to anisotropy at different length scales.[9–13] Of particular interest for the purpose of this study is a special case of the multiple-PFG acquisitions, where two pairs of gradients are employed and the delay or mixing time between the successive gradient pairs is short. In such double-PFG acquisitions, the signal is sensitive to microscopic anisotropy (μA), which is induced by the walls restricting the motion of molecules. This anisotropy is present even in isotropic

* Correspondence to: E. Özarslan, Section on Tissue Biophysics and Biomimetics, Program on Pediatric Imaging and Tissue Science, Eunice Kennedy Shriver National Institute of Child Health and Human Development, National Institutes of Health, Bethesda, MD 20892, USA. E-mail: evren@helix.nih.gov

a Section on Tissue Biophysics and Biomimetics, Program on Pediatric Imaging and Tissue Science, Eunice Kennedy Shriver National Institute of Child Health and Human Development, National Institutes of Health, Bethesda, MD 20892, USA

b Center for Neuroscience and Regenerative Medicine, Uniformed Services University of the Health Sciences, Bethesda, MD 20814, USA

c Mouse Imaging Facility, National Institute of Neurological Disorders and Stroke, National Institutes of Health, Bethesda, MD 20892, USA

† This article is published in Magnetic Resonance in Chemistry as a special issue on Magnetic Resonance in Food-Dealing with Complex Systems, edited by Belton and Capozzi.

Magn. Reson. Chem. 2011, 49, S79–S84   Published 2012. This article is a U.S. Government work and is in the public domain in the USA.

S79

pores.[14] The resulting angular dependence of the double-PFG signal is characterized by a bell-shaped curve from which the presence of restrictions to diffusion is inferred. The size of the compartments can be obtained by fitting an appropriate model to data. Because this angular dependence emerges in the quadratic term of a Taylor expansion of the NMR signal decay, restricted diffusion can be characterized, and microscopic dimensions can be measured using small gradient strengths. Such angular dependence has been observed in a radish specimen.[15]

In this work, we demonstrate the application of the double-PFG MRI technique to measure the diameter of cylindrical pores of microscopic dimensions and adopt the technique to measure the cell size in plants. First, a description of the employed theory, which involves incorporating the DTI-derived fiber orientation in a previously developed double-PFG framework is presented. Next, the double-PFG imaging sequence is introduced. The technique is subsequently validated through experiments on a stack of controlled glass capillary arrays (GCAs) with each wafer having different pore sizes to illustrate the contrast in the computed diameter maps. Finally, the method is applied to measure the size of phloem and xylem cells making up the vascular tissue of the celery stalk.

Methods

Overview of theory

There are two main approaches taken to relate the microstructural features of the specimen to the double-PFG MR observations of restricted diffusion. Continuing the work of Mitra,[3] the first approach treats the data as if they were acquired by setting the timing parameters to their limiting values.[15,16] More specifically, the duration of the gradient pulses (δ) is assumed to be infinitesimally short, while the separation of the pulses (Δ) is assumed to be sufficiently long for the molecules to traverse distances large compared to the dimension of the compartment they reside in. These assumptions greatly simplify the analysis. For example, when the separation between the two encoding blocks (mixing time) is zero, the small-q behavior ($q = |\mathbf{q}|$, where $\mathbf{q} = (2\pi)^{-1}\gamma\delta\mathbf{G}$, γ is the gyromagnetic ratio, and $\mathbf{G}$ is the gradient vector) of the MR signal attenuation is given by[3] $E(\psi) = 1-4\pi^2 q^2 \rho^2/3\ (2 + \cos(\psi))$, where ρ^2 is related to the mean-squared radius of gyration of the pores, and ψ is the angle between the two gradients. Frequently, one encounters pore shapes that can be characterized by a single size. For example, many biological cells are nearly spherical or cylindrical. In this case, the ρ^2 value can be related to the actual diameter of the pores. For cylinders, the signal modulation is given simply by $E(\psi) = 1-\pi^2 q^2 r^2\ (2 + \cos(\psi))$, where r is the radius of the cylinders. However, this expression is valid only when the special conditions for the timing parameters can be met, which is difficult to satisfy in practice.

In contrast, the second approach employs the assumption for the pore shape from the outset. This approach has enabled the incorporation of all timing parameters into the formalism,[9] thus significantly improving the size estimates.[17,18] The corresponding expressions are relatively complicated and will not be reproduced here.

Another important improvement is the extension of the formalism to arbitrary q-values. To this end, a theoretical framework that is valid for arbitrary gradient waveforms would be exceptionally useful. Such a theory was introduced by Özarslan *et al.*[19] It generalizes the multiple correlation function method[20] to pulse sequences that involve gradients applied along different

directions. This generalization is critically important for the multiple-PFG sequences where the gradients along different orientations are applied in different PFG blocks. Moreover, it opens the door to incorporate the effects of other gradients in the sequence such as spoilers and imaging gradients.

In this framework, a general gradient waveform is expressed as a piecewise constant function involving N separate intervals. A diagonal infinite-dimensional matrix operator, Λ, and a vector operator, $\mathbf{A}$, are constructed whose components are given by infinite-dimensional matrices, though finite-sized matrices are employed in practice. The elements of these operators are related to the eigenvalues of the Laplacian operator and the size of the pore. Then, the MR signal attenuation due to restricted diffusion is given simply by the very first element of the matrix

$$\prod_{n=1}^{N} \exp(-\delta_n \Lambda + i2\pi\mathbf{q_n}\cdot\mathbf{A}) \qquad (1)$$

where δ_n is the duration of the nth interval, and $\mathbf{q}_n$ is the corresponding $\mathbf{q}$-vector. Equation 1 enables one to compute the signal attenuation for simple geometries. The elements of the operators Λ and $\mathbf{A}$ for spherical and cylindrical pore shapes are provided elsewhere[19] and will not be reproduced here for brevity. This procedure enables one to compute the MR signal attenuation due to restricted diffusion for any pulse sequence as long as the gradients are applied in a direction perpendicular to the walls of the enclosing surface.

Of particular interest for the purposes of this study is the cylindrical geometry wherein the orientation of the cylinder should be taken into account. As shown before,[12] decomposing the $\mathbf{q}$-vector into components parallel with ($q_\parallel$) and perpendicular to ($\mathbf{q}_\perp$) the cylinder's symmetry axis makes it possible to write the attenuation due to diffusion within the cylinder as the product of two attenuations, i.e.,

$$E_r = E_\perp(\mathbf{q}_\perp)E_\parallel(q_\parallel). \qquad (2)$$

Here, $E_\perp(\mathbf{q}_\perp)$ can be computed using Eq. 1 as described above. As for $E_\parallel(q_\parallel)$, using the corresponding expression for a slab geometry would yield the signal attenuation for diffusion taking place inside a capped cylinder.[12,21] Alternatively, if the cylinders are very long so that diffusion is not influenced significantly by the presence of the caps, an infinite cylinder model could be used. In this paper, we follow the latter option, in which case the $E_\parallel(q_\parallel)$ function can be derived from the solution for free diffusion, denoted by E_f. The procedure to obtain E_f is well-known for arbitrary pulse sequences.[22] For example, when applied to the double-PFG sequences with vanishing mixing times, the relevant expression is given by[9]

$$E_f(\mathbf{q}_1, \mathbf{q}_2) = \exp(-4\pi^2 D_0[(\Delta - \delta/3)(q_1{}^2 + q_2{}^2) \qquad (3)$$
$$-(\delta/3)q_1 q_2 \cos(\psi)]),$$

where D_0 is the bulk diffusivity of the molecules, $\mathbf{q}_1$ and $\mathbf{q}_2$ are, \respectively, the $\mathbf{q}$-vectors associated with the first and second blocks of the double-PFG acquisition, and $q_1 = |\mathbf{q}_1|$ and $q_2 = |\mathbf{q}_2|$. Therefore, as a special case of the above expression,

$$E_\parallel(q_\parallel) = \exp(-4\pi^2 D_0[(\Delta - \delta/3)(q_{1\parallel}{}^2 + q_{2\parallel}{}^2)]) \qquad (4)$$
$$-(\delta/3)q_{1\parallel} q_{2\parallel}]),$$

where $q_{1\parallel}$ and $q_{2\parallel}$ are, respectively, the components of the vectors $\mathbf{q}_1$ and $\mathbf{q}_2$ along the cylinder's axis.

It is possible for a voxel to contain freely diffusing water molecules in addition to those confined to restricted domains. In this case, the above formulation for restricted diffusion can be combined with the expected signal behavior for free diffusion[9] in a bicompartmental model.[23] The aggregate signal is then given by $E = f_r E_r + f_f E_f$, where E_r and E_f are the signal attenuations from restricted and free domains, respectively, and f_r and f_f are the corresponding volume fractions that sum up to unity. It should be noted that this model assumes two populations of molecules to be non-exchanging, i.e., isolated from each other. Although this is an idealization of the diffusion process for many complex systems, the values obtained by employing such a model is expected to be meaningful when the exchange rate between the different pools is limited. When a substantial level of exchange is expected during the course of the diffusion encoding, a more sophisticated method that accounts for the permeability of membranes could be useful.[24]

Double-PFG MR pulse sequence

We illustrate the double-PFG filtered MRI pulse sequence[18] employed in this study in Figure 1. In this pulse sequence, double-PFG encoding is performed as a filter prior to spatial encoding.[25] Since we are interested in microscopic anisotropy, we would like to minimize the delay between the two diffusion blocks of the double-PFG sequence. This is achieved by applying the second gradient of the first pair simultaneously with the first gradient of the second pair. Thus, the resulting sequence has three pulses (of duration δ) where the separation of the successive gradient pulses is denoted by Δ. $\mathbf{G}_1$ and $\mathbf{G}_2$ are the gradient vectors of the two encodings. The second gradient of the three-pulse sequence is given by the vector sum $\mathbf{G}_1 + \mathbf{G}_2$. Once the

diffusion encoding is performed, the spatial encoding starts, which is achieved via slice selection as well as phase and frequency encoding.

Experiments and Results

Glass capillary array (GCA)

We performed double-PFG experiments on a diffusion MRI phantom[18] built from four stacked glass capillary array wafers (Photonis, Sturbridge, MA) filled with pure water. The phantom consisted of GCAs with a disk diameter of 13 mm and nominal pore diameter values of 25 and 10 μm (stacked in an alternating manner) with a maximum variation of 5% between GCAs of the same nominal diameter. MR acquisition was carried out on a 7 T vertical-bore Bruker DRX system (Bruker BioSpin, Billerica, MA, USA). The sample temperature was set to 19 °C. The double-PFG parameters were: δ/Δ = 3.15/75 ms, q-values of 9.9, 13.9, 19.8, 23.8 and 29.7 mm⁻¹ were achieved by applying gradients of strength 74, 103, 148, 177, and 221 mT/m. The sample was placed parallel to the main magnetic field, which defines the z-axis. The first gradient was fixed along the x-axis while the direction of the second gradient was varied on the transverse (xy) plane such that the angles between the two gradients (ψ) were 0, 45, 90, 135, 180, 225, 270, 315 and 360 degrees. In addition, one data set with no diffusion gradients was collected. The delay between the diffusion and spatial encoding sections of the pulse sequence was set to 35 μs. The parameters for the latter section were: TE/TR = 12/7000 ms, slice thickness = 2 mm, field of view = 15.5 mm, matrix size = 128x128, resolution = 121x121x2000 μm³. The number of averages was 2, yielding a total acquisition time of 30 minutes for each image.
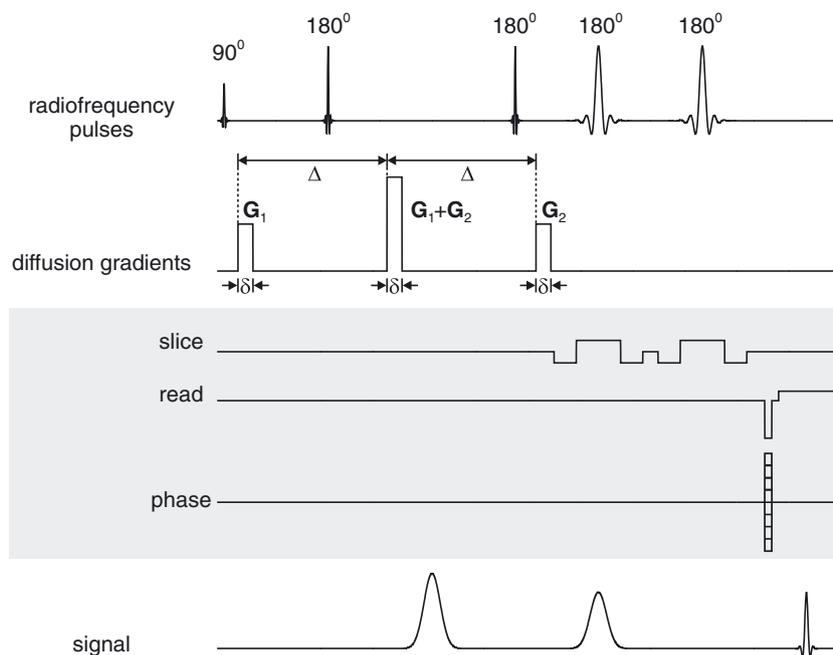

Figure 1. The double-PFG filtered MRI pulse sequence employed in this study. The sequence starts with a double-PFG diffusion encoding part that features hard radiofrequency (RF) pulses. Diffusion encoding is provided by a series of three gradient pulses of duration δ, while the separation of the successive gradient pulses is given by Δ. The magnitude and the direction of the two gradients of the double-PFG encoding are specified by the vectors $\mathbf{G}_1$ and $\mathbf{G}_2$ where the second gradient pulse is defined by the vector sum $\mathbf{G}_1 + \mathbf{G}_2$. Therefore, the sequence can be thought of to be comprising two pairs of gradients with no mixing time between the respective pairs. The double-PFG encoded magnetization is subsequently fed into a standard imaging sequence with soft RF pulses to enable slice selection. The resulting signal, hence both diffusion and spatially encoded, is used to reconstruct the double-PFG MR images.

wileyonlinelibrary.com/journal/mrc

S81

In Figure 2, we illustrate our experimental results on the GCA phantom. The top row of this figure contains four double-PFG images, two at a low q-value and two at the highest q-value. In both cases, images with parallel ($\psi = 0^0$) and antiparallel ($\psi = 180^0$) gradients are included. Clearly, at the higher q-value, there is a significant attenuation of the signal in the parallel case relative to the case in which gradients are oriented antiparallel. Note that this anisotropy of the signal is not due to the pores being elongated, as the gradients are perpendicular to the walls of the pore in all cases. Rather, it is induced by the mere presence of the walls, and as such, it is indicative of their reflective character. The arrows indicate the location from which the signal values are plotted on the right. In this plot, the symbols indicate the data points while the fit to these points are depicted via continuous lines.

The fits were obtained by computing the signal values using the theoretical framework outlined above. The unknown parameters to be estimated via the fitting were: the radius of the cylinders, and the signal values with no diffusion weighting corresponding to the restricted and free compartments, which we shall denote by S_{0r} and S_{0f}, respectively. Note that the aggregate signal with no diffusion weighting is just sum of these two signal intensities, i.e., $S_0 = S_{0r} + S_{0f}$. The volume fractions of the two compartments are also obtained from these signal intensities via the relationships $f_{0r} = S_{0r}/S_0$ and $f_{0f} = S_{0f}/S_0$. An IDL implementation of the Levenberg-Marquardt algorithm available at http://www.physics.wisc.edu/~craigm/idl/fitting.html was employed in the fitting, which also provided error estimates in the results.

In the bottom row of Figure 2, we illustrate the results obtained via voxel-by-voxel fitting of the model to the data. The first image is a map of the estimated inner diameter (ID) values. A region of interest analysis over the respective GCAs revealed inner diameter values of 27.1 ± 0.4, 10.0 ± 0.7, 27.3 ± 0.4, $10.2 \pm 0.6\,\mu m$ for the voxel-by-voxel pore size estimates. The fitting of the theory to the values obtained by averaging the signal values over the

same regions within each of the GCAs led to estimates of 27.36 ± 0.12, 10.04 ± 0.08, 27.43 ± 0.14, $10.17 \pm 0.08\,\mu m$ for the pore diameter. Note that all these values are reasonably close to their nominal values. Moreover, the consistency of the results obtained from the voxel-by-voxel analysis with that achieved by averaging the signal values prior to fitting indicates the adequacy of the signal level for a local estimate of the pore diameter. The image with no-diffusion weighting (S_0) obtained from the fit is shown in the second map of the bottom row in Figure 2. Unlike in the case of the ID-valued map, the S_0 image does not yield significant contrast between the GCAs with vastly different pore diameters. The last two figures depict the restricted and free volume fractions (f_r and f_f), which are useful in distinguishing regions containing freely diffusing water from those with restricted diffusion.

Celery

We used a similar framework to image a specimen of celery stalk inside water. The MRI protocol included a series of 18 double-PFG scans followed by a diffusion tensor imaging (DTI)[26] protocol with 44 single-PFG spin echo acquisitions. The parameters for the DTI acquisition were: TE/TR = 59/3000 ms, δ/Δ = 3/50 ms, field of view = 22 mm, matrix size = 128x128, resolution = 172x172x2000 mm^3. Two images with no diffusion gradients were acquired followed by 42 diffusion weighted images (21 directions, 2 b-values up to 340 s/mm^2, where $b = 4\pi^2 q^2(\Delta-\delta/3)$). The number of averages was 1, and the total acquisition time was 4 hours and 42 minutes.

Double-PFG filtered imaging was performed on the same geometry. The double-PFG parameters were: TE/TR = 12/3000 ms, δ/Δ = 3.15/50 ms. A total of eighteen double-PFG images were acquired, one at $q = 0\,mm^{-1}$, three at $q = 9.9\,mm^{-1}$ and seven images were collected at each of $q = 13.9$ and $19.8\,mm^{-1}$. The number of averages was 8, yielding a total acquisition time of 51 minutes for each image.
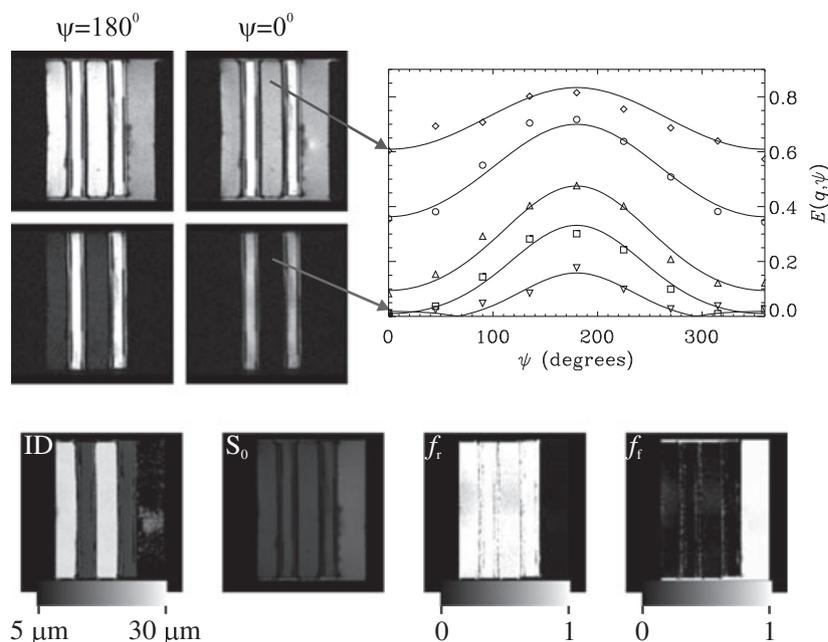

Figure 2. The results obtained from the experiments on the glass capillary array (GCA) phantom. On the top row, 4 of the 46 double-PFG images are shown. The signal profiles (5 q-values and 9 angles) for a randomly selected voxel are shown on the plot where the continuous curves depict the theoretical fit to the data. The bottom row illustrates the quantitative maps of cylinder inner diameter (ID), the image with no diffusion-weighting (S_0), and the restricted and free volume fractions (f_r and f_f).
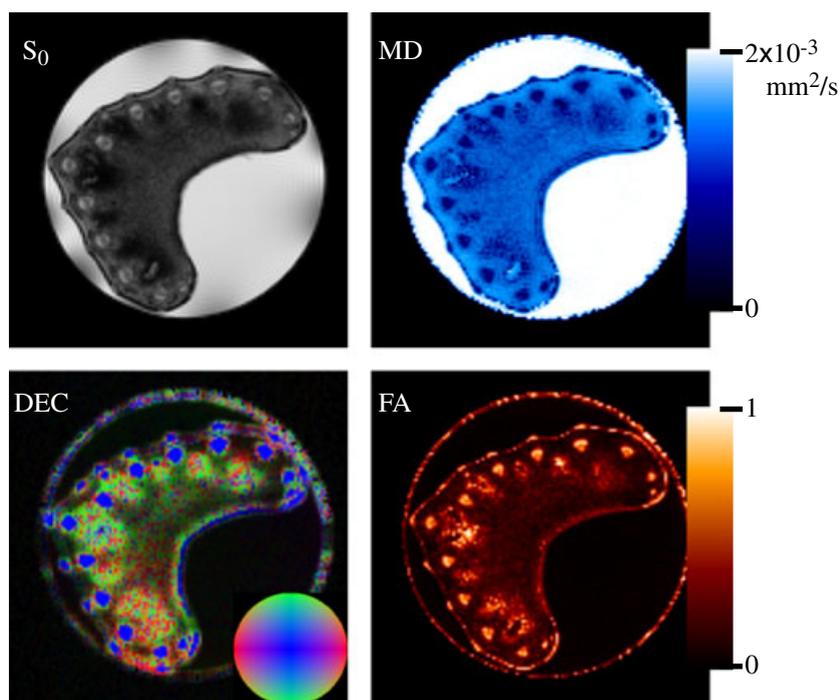
Figure 3. DTI-derived parameters of the image with no diffusion weighting (top left), mean diffusivity (top right), and fractional anisotropy maps (bottom right) along with the direction encoded color map (bottom left) depicting the orientation associated with the primary eigenvalue of the diffusion tensor. In this panel, red, green and blue colors depict the right-left, up-down and through the page orientations, respectively.

In Figure 3, we illustrate the images obtained from the DTI acquisition. Specifically, we show the image with no diffusion weighting and the quantitative maps of mean diffusivity (MD) and fractional anisotropy (FA).[27] The figure on the bottom left corner depicts the direction encoded color (DEC) map[28] obtained from the principal eigenvector of the diffusion tensor. This map shows the primary orientation of the fibers within each voxel. Note the sharp contrast the vascular bundles yield in DEC and FA maps suggesting the coherence and elongation of the cells in these regions. Moreover, in these regions, the cells appear to be oriented in-and-out of the image plane as expected.

In this study, these DTI findings were exploited for two purposes: (i) Due to the realization of the sharp contrast in the direction encoded color (DEC) maps between the vascular and the surrounding tissue, the voxels that are contained in the manually drawn ROIs were further pruned by excluding those with fiber orientations making an angle larger than 15^0 with the z-axis. (ii) Any small deviation of the orientation of the cells from the z-axis was accounted for by feeding the DTI-derived orientation into the double-PFG fitting procedure as a priori information. Consequently, the diffusion gradients, which are applied on the xy-plane, are decomposed into two components, one along the fiber and one perpendicular to it as described in the Theory section. The former component thus leads to signal attenuation consistent with free diffusion, while for the latter the solution for restricted diffusion was employed. Apart from this important difference, the fitting procedure followed similar lines as for the GCA data set. The unknown parameters that were determined via the fitting procedure were the fiber radius, S_{0r}, S_{0f}, and the bulk diffusivity, D_0. One double-PFG scan with low diffusion-weighting is illustrated in Figure 4. A region-of-interest (ROI) was drawn manually that includes each of the regions containing the vascular bundles; these regions were later pruned via the
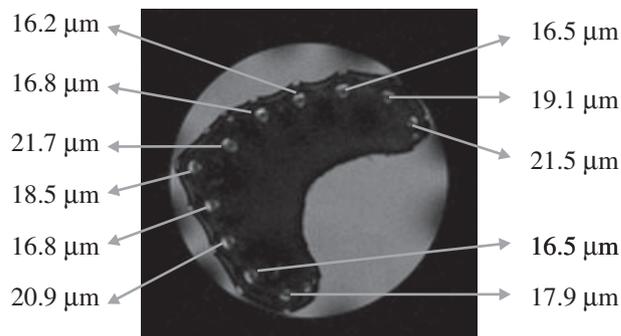

Figure 4. A double-PFG MR image of a celery stalk. The numbers indicate the diameter estimates for the cells within the vascular regions of the celery.

DTI-derived DEC map as mentioned above. The signal values were averaged over the respective ROIs. The values obtained from the fitting can be seen in Figure 4 as well. The estimates are consistent with their expected values.

Discussion and Conclusion

It is instructive to consider traditional (k-space) MR imaging as another potential method to directly image the pore space and measure the size of the compartments from such images. However, it is impossible to resolve the individual cylinders using our instrument since, due to the size of the specimens (GCAs or celery stalk), such very high resolution scans would demand a very large matrix size, hence prohibitively long acquisition times. Further, the loss of SNR is expected to be another major limiting factor in such acquisitions. As described in this work, by exploiting the diffusion of molecules and its influence on the double-PFG method, we were

able to measure the diameter of the cylinders with reasonable accuracy and precision.

Double-PFG MR is a promising new alternative to more traditional single-PFG acquisitions that provides novel information while making more modest demands on the gradient hardware. For example, to probe different length scales via single-PFG scans one could vary the diffusion pulse separation.[29] On the other hand, because two pairs of gradients are employed in double-PFG acquisitions, two new experimental parameters (the delay between the two pairs, and the angle between the two gradients) can be systematically varied as well. Of particular interest in this study was the short separation time experiments, which are sensitive to restricted diffusion at very low q-values. Consequently, such data can be acquired even when strong gradient coils are not available and the microstructural features of the specimen can still be obtained.

This paper employed a theoretical framework that we presented in a series of articles, and extended it by incorporating the fiber orientation. Although the fiber orientation can be determined from the double-PFG acquisitions as well, it would require a gradient sampling scheme more sophisticated than the circular sampling employed in this work. Here, the deviation of the vascular fiber orientation from the z-axis was assumed to be small, which made it possible to estimate the size of the cells by using the circular sampling scheme even when the plane of the sampled circle is not perfectly perpendicular to the fiber direction. This small deviation can be obtained via an independent method—in the present application, that method was a DTI acquisition performed in tandem. Other contributions of the paper included the illustration of a sharp size-dependent contrast in a well-controlled phantom of GCAs, and the application of our method to a plant tissue.

The validation of the technique involved experiments on a phantom comprising glass capillary arrays (GCAs). Subsequently, the method was applied to quantify the size of phloem and xylem cells—the two main constituents of the vascular tissue in celery stalk. Considering that incorporation of fast imaging techniques like echo planar imaging (EPI) would considerably shorten the acquisition times, the satisfactory results of this study combined with the less demanding nature of the double-PFG experiments suggest it as a feasible non-invasive method to characterize the microstructure of vascular plant cells, which are implicated in the transport of water and nutrients along the plant stem. Moreover, the technique is expected to be useful in tackling other problems in food science such as characterizing the size of droplets in emulsions[30] (e.g., cheese and margarine[31]).

Acknowledgments

Conflicts of interest

The authors declare no conflicts of interest.

References

[1] E. O. Stejskal, J. E. Tanner, *J. Chem. Phys.* **1965**, *42*, 288–292.
[2] D. G. Cory, A. N. Garroway, J. B. Miller, *Polym. Prepr.* **1990**, *31*, 149.
[3] P. P. Mitra, *Phys. Rev. B* **1995**, *51*, 15074–15078.
[4] Y. Cheng, D. G. Cory, *J. Am. Chem. Soc.* **1999**, *121*, 7935–7936.
[5] P. T. Callaghan, I. Furó, *J. Chem. Phys.* **2004**, *120*, 4032–4038.
[6] Y. Qiao, P. Galvosas, P. T. Callaghan, *Biophys. J.* **2005**, *89*, 2899–2905.
[7] P. T. Callaghan, A. Coy, D. MacGowan, K. J. Packer, F. O. Zelaya, *Nature* **1991**, *351*, 467–469.
[8] E. Özarslan, P. J. Basser, *J. Magn. Reson.* **2007**, *188*, 285–294.
[9] E. Özarslan, P. J. Basser, *J. Chem. Phys.* **2008**, *128*, 154511.
[10] M. E. Komlosh, F. Horkay, R. Z. Freidlin, U. Nevo, Y. Assaf, P. J. Basser, *J. Magn. Reson.* **2007**, *189*, 38–45.
[11] J. Finsterbusch, *J. Magn. Reson.* **2009**, *198*, 174–182.
[12] E. Özarslan, *J. Magn. Reson.* **2009**, *199*, 56–67.
[13] J. Finsterbusch, in Annual Reports on NMR Spectroscopy (Ed: G. A. Webb), Academic Press, Burlington, **2011**, pp. 225–299.
[14] E. Özarslan, U. Nevo, P. J. Basser, *Biophys. J.* **2008**, *94*, 2809–2818.
[15] M. A. Koch, J. Finsterbusch, *Magn. Reson. Med.* **2008**, *60*, 90–101.
[16] T. Weber, C. H. Ziener, T. Kampf, V. Herold, W. R. Bauer, P. M. Jakob, *Magn. Reson. Med.* **2009**, *61*, 1001–1006.
[17] N. Shemesh, E. Özarslan, P. J. Basser, Y. Cohen, *J. Magn. Reson.* **2009**, *198*, 15–23.
[18] M. E. Komlosh, E. Özarslan, M. J. Lizak, F. Horkay, V. Schram, N. Shemesh, Y. Cohen, P. J. Basser, *J. Magn. Reson.* **2011**, *208*, 128–135.
[19] E. Özarslan, N. Shemesh, P. J. Basser, *J. Chem. Phys.* **2009**, *130*, 104702.
[20] D. Grebenkov, *Rev. Mod. Phys.* **2007**, *79*, 1077–1137.
[21] Y. Assaf, R. Z. Freidling, G. K. Rohde, P. J. Basser. *Magn. Reson. Med.* **2004**, *52*, 965–978.
[22] P. T. Callaghan, Principles of Nuclear Magnetic Resonance Microscopy, Clarendon, Oxford, **1991**.
[23] N. Shemesh, E. Özarslan, A. Bar-Shir, P. J. Basser, Y. Cohen, *J. Magn. Reson.* **2009**, *200*, 214–225.
[24] D. S. Grebenkov, *J. Magn. Reson.* **2010**, *205*, 181–195.
[25] M. E. Komlosh, M. J. Lizak, F. Horkay, R. Z. Freidlin, P. J. Basser, *Magn. Reson. Med.* **2008**, *59*, 803–809.
[26] P. J. Basser, J. Mattiello, D. LeBihan, *J. Magn. Reson. B* **1994**, *103*, 247–254.
[27] P. J. Basser, C. Pierpaoli, *J. Magn. Reson. B* **1996**, *111*, 209–219.
[28] S. Pajevic, C. Pierpaoli, *Magn. Reson. Med.* **1999**, *42*, 526–540.
[29] E. Özarslan, P. J. Basser, T. M. Shepherd, P. E. Thelwall, B. C. Vemuri, S. J. Blackband, *J. Magn. Reson.* **2006**, *183*, 315–323.
[30] K. J. Packer, C. Rees, *J. Colloid Interface Sci.* **1972**, *40*, 206–218.
[31] P. T. Callaghan, K. W. Jolley, R. S. Humphrey, *J. Colloid Interface Sci.* **1983**, *93*, 521–529.